

21-54
39622

Distorted turbulence submitted to frame rotation: RDT and LES results

By Fabien S. Godeferd¹

1. Motivation and objectives

The stability analysis of homogeneous turbulence submitted to mean velocity gradients can be investigated from a pure mathematical point of view by examining the growth of a single Fourier mode as a perturbation to a background flow. The engineering method of studying the same flow is to use Rapid Distortion Theory (RDT) applied to a group of Fourier modes that represent a more "physical" turbulent flow. However, both approaches deal with the amplification or damping coefficients that arise from the linearized equations. Comparison of simple RDT approximation to the more costly Direct Numerical Simulation (DNS) has led to good agreement, at least qualitatively, in terms of structure between predictions of sheared homogeneous turbulent flow through RDT and results of simulations of a stationary channel flow (Lee, Kim & Moin, 1990). They find that the shear induced by the mean velocity profile close to the walls is the main factor for this agreement. Starting from a purely isotropic flow, streak-like structures appear in sheared homogeneous flows, even in the linear approximation. The objective of this effort is to carry the analysis of Lee *et al.* (1990) to the case of shear with rotation. We apply the RDT approximation to turbulence submitted to frame rotation for the case of a uniformly sheared flow and compare its mean statistics to results of high resolution DNS of a rotating plane channel flow. In the latter, the mean velocity profile is modified by the Coriolis force, and accordingly, different regions in the channel can be identified. The properties of the plane pure strain turbulence submitted to frame rotation are, in addition, investigated in spectral space, which shows the usefulness of the spectral RDT approach. This latter case is investigated here. Among the general class of quadratic flows, this case does not follow the same stability properties as the others since the related mean vorticity is zero.

2. RDT equations in spectral space

2.1 Basic equations

We consider here incompressible homogeneous turbulence with total velocity field $\mathbf{U}(\mathbf{x}, t) = \overline{\mathbf{U}}(\mathbf{x}) + \mathbf{u}(\mathbf{x}, t)$, where \mathbf{u} is the fluctuating velocity and $\overline{\mathbf{U}}$ is the mean velocity. The mean velocity is taken to be independent of time with uniform uniform gradient in space. Therefore, only the mean velocity gradients $\overline{U}_{i,j} = \overline{G}_{ij}$ appear in the equations. The flow is set in a rotating frame with angular velocity vector

¹ LMFA/URA CNRS 263 – École Centrale de Lyon – France

Ω^f , and the classical symmetric/skew symmetric decomposition is performed on the mean velocity gradients tensor

$$S_{ij} = (\overline{U}_{i,j} + \overline{U}_{j,i}) / 2$$

and

$$W_{ij} = (\overline{U}_{i,j} - \overline{U}_{j,i}) / 2 .$$

The rotation tensor is related to the vorticity through $\mathbf{W}_{ij} = 1/2 \epsilon_{ijk} \Omega_k$. The rapid distortion approximation is obtained by dropping the nonlinear terms in the Navier-Stokes equations. Using the previously introduced decomposition for the mean velocity gradients, we get the corresponding linearized equation, which, for a non viscous fluid, reads

$$\dot{\mathbf{u}} = \partial_t \mathbf{u} + \overline{U}_j \partial_j u_i = -\mathbf{S} \cdot \mathbf{u} - (\Omega + 2\Omega^f) \times \mathbf{u} - \nabla p \quad (1)$$

where the equations are written in the rotating frame Ω_k . In this frame, a general method of decomposition for homogeneous sheared flows is used by considering the expansion of the fluctuating fields in terms of time-dependent Fourier modes $\exp(i\mathbf{k}(t) \cdot \mathbf{x})$, where the wave vectors evolve in time according to $\partial_t \mathbf{k}_i = -\overline{U}_{j,i} k_j$. The Lagrangian wave vectors \mathbf{K} , which are associated with the Lagrangian physical coordinates \mathbf{X} that follow the distortion of the flow, are related to the Eulerian ones by the relation

$$\mathbf{k} \cdot \mathbf{x} = \mathbf{K} \cdot \mathbf{X} .$$

These variables, (\mathbf{X}, \mathbf{K}) , which follow the deformation of the space, have been used by Cambon *et al.* (1985) and are exactly the same as the Rogallo space variables (Rogallo, 1981).

2.2 Solutions in the Craya-Herring local frame

In the following, we shall take advantage of the Craya-Herring decomposition of the fluctuating velocity $\hat{\mathbf{u}}$ (Craya, 1958, Herring, 1974) by choosing a given direction in the flow along a vector \mathbf{n} . This decomposition uses a local frame of reference in the plane perpendicular to the wave vector \mathbf{k} . The Fourier transformed velocity $\hat{\mathbf{u}}$ is such that $\mathbf{k} \perp \hat{\mathbf{u}}$ from the continuity equation $\mathbf{k} \cdot \hat{\mathbf{u}} = 0$. The first component of $\hat{\mathbf{u}}$ in this frame is its projection $\hat{\varphi}^1$ onto the "equatorial" vector $\mathbf{e}_1 = \mathbf{k} \times \mathbf{n} / |\mathbf{k} \times \mathbf{n}|$, and its second component is the remaining part $\hat{\varphi}^2$, along $\mathbf{e}_2 = \mathbf{e}_1 \times \mathbf{k} / |\mathbf{e}_1 \times \mathbf{k}|$. We refer to \mathbf{n} as the *polar* direction and to the plane orthogonal to \mathbf{n} as the *equator*, since the $(\mathbf{e}_1, \mathbf{e}_2)$ frame is also the set of axes associated with spherical coordinates. The Fourier transformed fluctuating velocity can then be written as

$$\hat{u}_i(\mathbf{k}, t) = \hat{\varphi}_1(\mathbf{k}, t) e_i^1 + \hat{\varphi}_2(\mathbf{k}, t) e_i^2 .$$

Using these variables, the linearized evolution Eq. (1) can be rewritten, and one obtains the equations for each component of $\hat{\mathbf{u}}$ in the Craya-Herring frame

$$\dot{\hat{\varphi}}_n(\mathbf{k}, t) + m_{nl}(\mathbf{k}) \hat{\varphi}_l(\mathbf{k}, t) = 0 \quad (2)$$

where $k, l = 1, 2$ and the linear operator matrix

$$m_{nl} = S_{ij} (e_i^k e_j^l - \epsilon_{nl3} e_i^2 e_j^1) + \epsilon_{nl3} (\Omega_l + 2\Omega_l^f) \frac{k_l}{k}.$$

Note that m does not depend on the modulus of the wave vector, but only on its orientation. Therefore, the time evolution factors of the different modes of velocity $\hat{\varphi}_n(\mathbf{k}, t)$ are identical for all the wave vectors with the same orientation. The advantage of this procedure is to save computing time since the values of the amplification factors need be computed only for different orientations of a unit wave vector (*i.e.* a discretization of a sphere of radius unity) (Cambon, 1982, Benoit, 1992). These coefficients allow one to evaluate the time variation for all vectors in wave space. Once Eq. (2) is solved for a given set of initial conditions by way of a matrix exponential rather than inverting the linear system, the complete statistics in the flow can be computed easily without further computations. All of the statistics such as spectra of two-point correlations and, of course, one-point quantities are entirely known through the knowledge of the amplification coefficients and statistical quantities at the initial time. The whole method has been implemented in a code named MITHRA at the LMFA (Benoit, 1992).

Alternatively, Eq. (2) holds for all discretization of the spectral space, and we have been able to apply this method of resolution for wave vectors that are spread on a classical spectral cubic distribution, as for direct numerical simulations (see Section 4.3). The independence of the amplification of the different velocity modes with the modulus of the wave vector is no more valid when one considers a *viscous* fluids for which, of course, a dissipation term proportional to νk^2 appears in the equations.

Note that the distortion of the computing mesh in RDT and in DNS are the same but have a different impact on the accuracy of the computation. In the former approach, there is no flux of energy through the boundary of the resolved space. Therefore, no problem of resolving the different scales in the flow arises since the different scales are as well represented by the distorted mesh as they were in the initial one, at $t = 0$. If one now considers the DNS approach, there is a flux of energy through the boundaries of the resolution mesh, and a remeshing at given periodic intervals in time is necessary if one wants to keep as much resolved energy containing scales in the computational box as possible.

2.3 Linear stability results

We consider here a general type of deformation in the plane (1,2) with mean velocity gradients such that (quadratic flow),

$$\bar{G} = \begin{pmatrix} D & -\Omega \\ \Omega & D \end{pmatrix},$$

or equivalently

$$\bar{G} = \begin{pmatrix} 0 & D - \Omega \\ D + \Omega & 0 \end{pmatrix}$$

if the principal axes of the associated pure strain tensor S are chosen. Cambon *et al.* (1994) have confirmed that linear stability analysis gives a maximum destabilization for zero tilting vorticity $2\Omega^f + \Omega = 0$, whereas stability is found for zero absolute vorticity $2\Omega + 2\Omega^f = 0$.

In the case of simple uniform shear with rotation, the pressureless analysis by Bradshaw concluded with a stability governed by the Bradshaw-Richardson number $B = R(R + 1) > 0$, with $R = 2\Omega^f/S$ or $B = 2\Omega^f(2\Omega^f - S)/S^2 > 0$. The maximum growth rate of the unstable case is obtained for $B = -1/4$ (or equivalently $R = -1/2$). In the general case for given Ω^f and D , Salhi & Cambon (1995b) have shown the validity of the extended criterion $B = D^2 - (2\Omega^f - \Omega)^2$.

Now that we have stated the stability criteria for the general case of distortions, we shall use it for studying the behavior of two specific cases, a purely strained and a sheared turbulence.

3. Purely strained homogeneous turbulence in a rotating frame

The case of a plane pure strain applied to the flow is one of the simplest, with a deformation tensor written as

$$G = \begin{pmatrix} D & 0 \\ 0 & D \end{pmatrix}$$

and $\Omega = 0$. No stability result can be obtained through the classic Bradshaw criterion for pure shear, for here Ω is zero. We expect the stability of the flow to depend upon the ratio of the two controlling parameters, namely $2\Omega^f/D$, the rotation number. The symmetry of the deformation implies independence of the results with the sign of the rotation rate Ω^f . Indeed, the pressureless analysis gives $B = D^2 - (2\Omega^f)^2$ (Salhi & Cambon, 1995b, Speziale *et al.*, 1995).

3.1 Stability analysis

We have computed the time evolution of the kinetic energy for different values of the rotation rate, which leads to the following simple linear stability result (Fig. 1): q^2 grows exponentially for $2\Omega^f/D < 1$ and is damped otherwise; the rotation of the frame applied to a plane pure strained flow is stabilizing only for high rotation rate. However, at very large values of the cumulative distortion Dt , even the latter cases may exhibit a growth of kinetic energy. In this case, the time scale is probably large enough so that the nonlinear terms can no longer be neglected.

The evolution of the enstrophy $\omega^2 = \langle \omega_i \omega_i \rangle$ (ω is the vorticity of the fluctuating flow) with the non-dimensional time t/T is shown in Fig. 2. $T = (2\pi/\Omega^f)$ is the characteristic time of the frame rotation. We find that the exponential growth occurs for *all values* of the rotation rate. But there is a clear separation in the growth rates of ω^2 between the stabilized cases and the destabilized ones (with respect to the kinetic energy).

For such a deformation, the growth rate of the kinetic energy should *a priori* be independent of the sign of the rotation applied to the flow. This symmetry condition is a good test of the accuracy of the numerical resolution method. Indeed, we see

in Fig. 1 that the q^2 evolutions for $2\Omega^f/D = 1$ and $2\Omega^f/D = -1$ begin to depart slightly around the value $Dt = 5$ for the cumulative distortion rate. Therefore, if we need to reach higher values, *e.g.* $Dt > 10$, with sufficient precision, a very large number of discretized points is necessary. This condition would be much more strenuous if we used a classical cubic discretization of the space rather than spreading the resolution points on a sphere of unit radius.

3.2 Production of kinetic energy

The behavior of the production term in the equation for kinetic energy depends on the value of the ratio $2\Omega^f/D$, reflecting the stabilizing or destabilizing role of the solid body rotation on the strained turbulent flow. We can compute the evolution in time of the only non-zero term $-\langle u_1 u_2 \rangle$, and investigate its proportion at a given instant t with respect to the kinetic energy at this instant. This *relative* value is a clue for understanding how the rotation modifies the production of kinetic energy. We can see from Fig. 3 that $-\langle u_1 u_2 \rangle$ is positive when the stability criterion $2\Omega^f/D > 1$ is not met, but also that the transition from this unstable regime to the stable one where $-\langle u_1 u_2 \rangle < 0$ is not smooth. This effect, possibly due to round-off errors, shows the degree of sensitiveness of the flow to the resolution method even though our numerical scheme here is of very high order and our resolution grid is very fine.

3.3 Full spectral distribution

The instability of the plane strained homogeneous turbulence under rotation is well reflected through the one-point quantity q^2 . However, the exponential growth of kinetic energy is the consequence of the amplification of an unstable region of wave vector orientations in spectral space. Accordingly, we have plotted in Figs. 5 and 6 the distribution of kinetic energy, and similarly in Fig. 4 that of the enstrophy, on a sphere of given radius. One can therefore identify the zone of maximum destabilization, or maximum amplification, of kinetic energy as being the wave vector orientations mainly responsible for the destabilization of the flow. The surface is initially a sphere, but is distorted when time evolves. However, our representation is Lagrangian, and therefore all the distributions are represented on a sphere. This kind of representation has been successfully used by Cambon *et al.* (1994) for concluding that only a very narrow band of wave vectors is destabilized in the case of the elliptical flow submitted to frame rotation. Figure 6 shows that no such peculiar orientation is present in the case of the strained turbulence. However, it shows that the most destabilized wave vectors are those orthogonal to the frame rotation vector, *i.e.* those that lie in the equatorial region of the sphere, since there is no explicit effect of the Coriolis force on these wave vectors. Equivalently, in physical space there is no influence of the Coriolis force on fluid motion that is parallel to the rotation vector. The unstable modes are all located in a band at an angle $\pi/4$ radians, where the longer the evolution time the thinner the band, along with the above mentioned concentration in the equatorial plane. The difference between Figs. 5 and 6 shows how the rotation tends to reduce the thinning of the instability band. The enstrophy, shown in Fig. 4, exhibits the same pattern as the

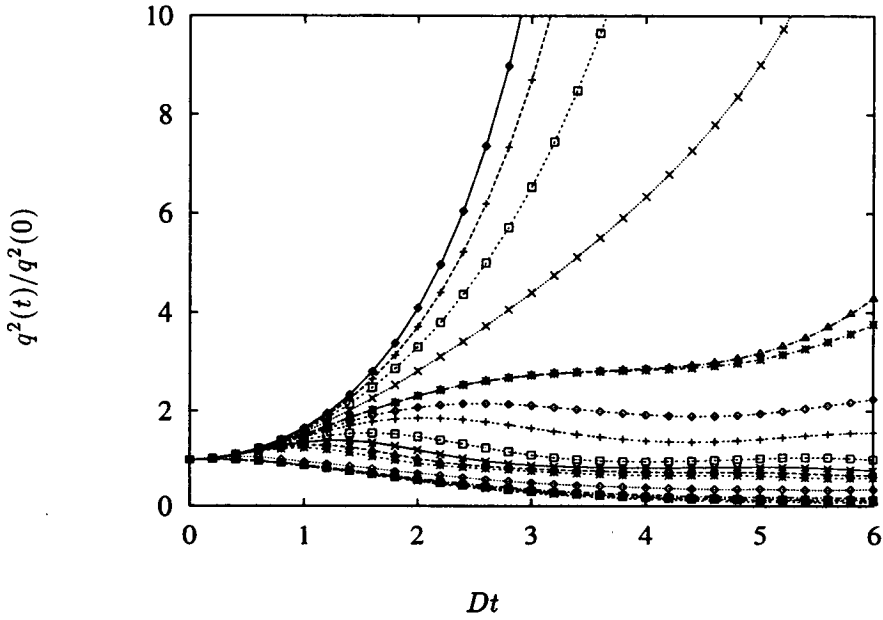


FIGURE 1. Normalized kinetic energy $q^2(t)/q^2(0)$ for different values of the rotation rate Ω^f , as a function of the non-dimensional time Dt . Curves clockwise from top of figure: $\Omega^f = 0, 0.2, 0.3, 0.4, -0.5, 0.5, 0.55, 0.6, 0.7, 0.8, 0.9, 1, 2, 5, 8, 10, 20$.

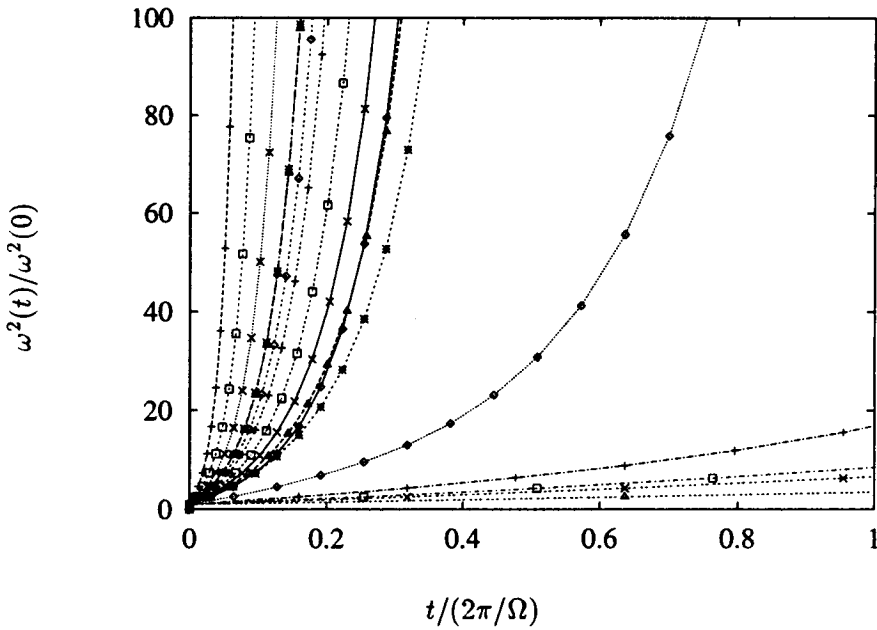


FIGURE 2. Normalized enstrophy $\omega^2(t)/\omega^2(0)$ for different values of the rotation rate Ω^f , as a function of the non-dimensional time $t/(2\pi/\Omega)$. The case at $\Omega^f = 0$ is non dimensionalized using $\Omega^f = 1$. Curves as in Fig. 1.

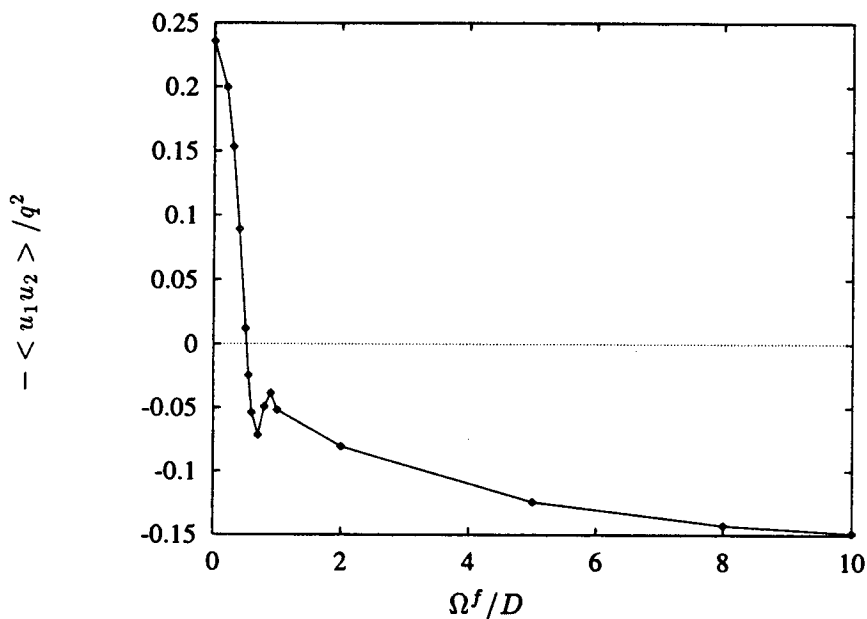


FIGURE 3. Normalized production of kinetic energy $-\langle u_1 u_2 \rangle / q^2$ at time $t = 3$ for different values of the ratio Ω^f/D .

kinetic energy distribution.

4. Sheared homogeneous turbulence in a rotating frame

We now go on to the case of sheared homogeneous turbulence for which the mean velocity gradients lead to the decomposition:

$$\mathbf{S} = \begin{pmatrix} 0 & D \\ D & 0 \end{pmatrix}$$

and

$$\mathbf{W} = \begin{pmatrix} 0 & -\Omega \\ \Omega & 0 \end{pmatrix}$$

with the particular choice $\Omega = D$. The resulting mean velocity gradient is $d\bar{U}_1/dy = 2D = S$.

4.1 Stability analysis

The general stability results have been briefly reviewed in Section 2.3 (see also Salhi & Cambon, 1995a). Accordingly, the evolution of the kinetic energy shows an exponential growth when the rotation of the frame does not compensate the vorticity induced by the shear, namely $2\Omega^f/S < 1$, as shown in Fig. 7.

But, looking only at the enstrophy growth rates (Fig. 8), it is not possible to distinguish the destabilized cases and the stabilized ones, as can be done in the case of the plane strain. The mechanism of enstrophy production is different in the two cases and is less affected by the rotation in a homogeneous shear flow.

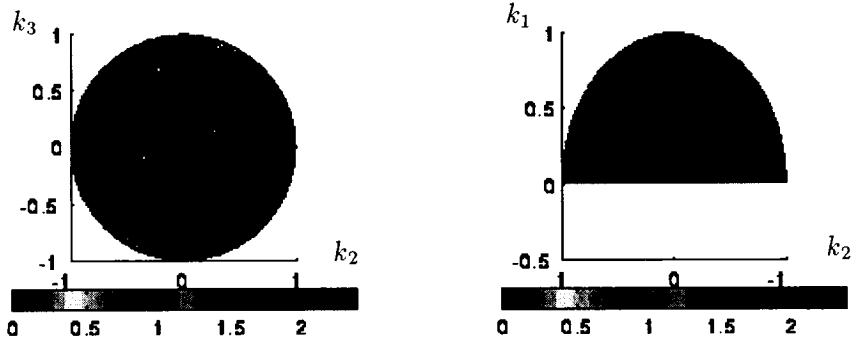


FIGURE 4. Full spectral distribution of the enstrophy ω^2 for a plane strained homogeneous turbulence with frame rotation $\Omega^f = 10$. Left figure: top view of the spectral sphere; right figure: side view. Snapshot taken at $Dt = 1.5$.

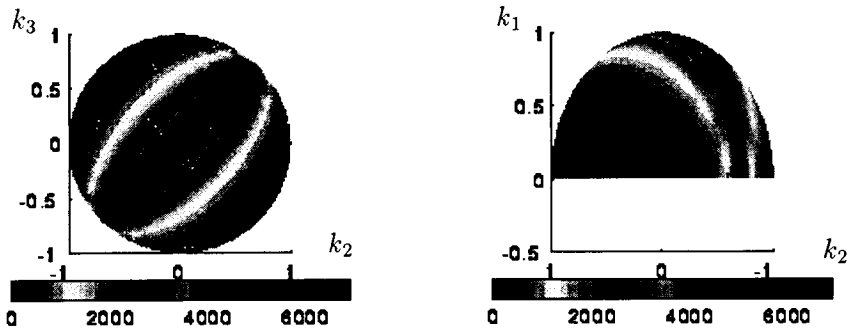


FIGURE 5. Full spectral distribution of the kinetic energy for a plane strained homogeneous turbulence with a rotation rate $\Omega^f = 0.2$. Left figure: top view of the spectral sphere; right figure: side view. Snapshot taken at $Dt = 1.5$.

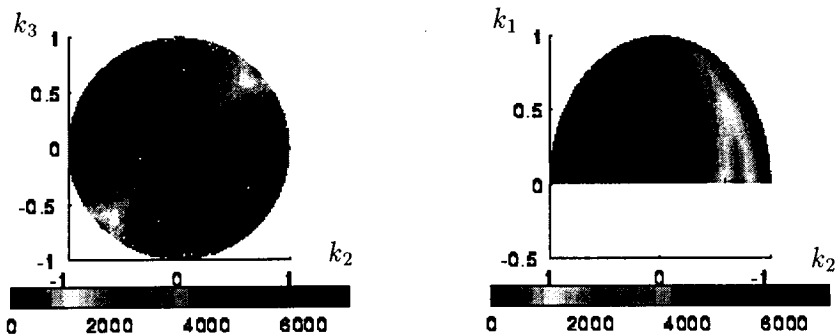


FIGURE 6. Full spectral distribution of the kinetic energy for a plane strained homogeneous turbulence with $\Omega^f = 10$. Left figure: top view of the spectral sphere; right figure: side view. Snapshot taken at $Dt = 1.5$.

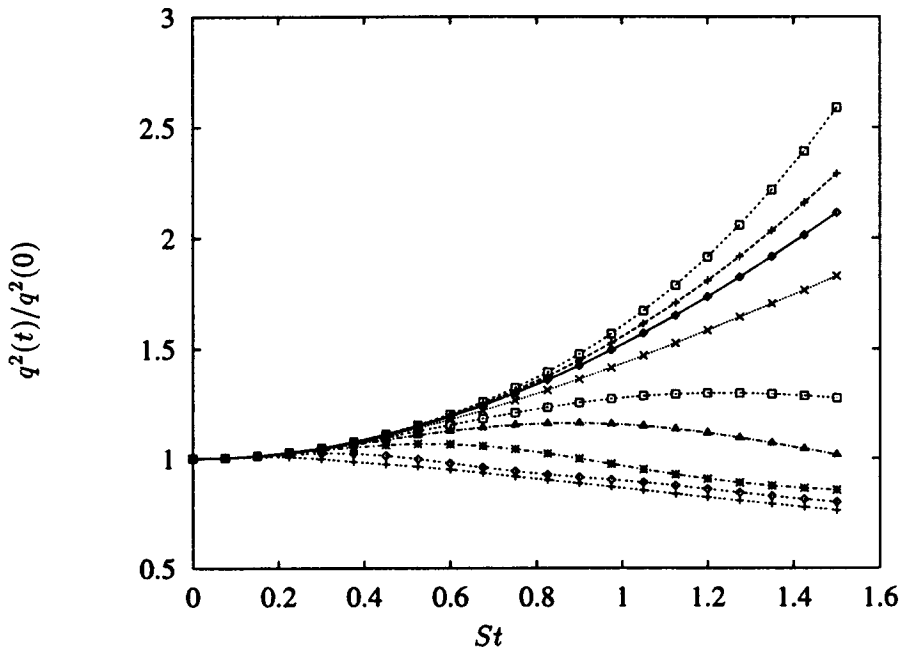


FIGURE 7. Normalized kinetic energy $q^2(t)/q^2(0)$ for different values of the rotation number $2\Omega^f/S$, as a function of the non-dimensional time St . Curves clockwise from top of figure: $2\Omega^f/S = -0.5, 0.1, 0, 1, 0.5, 1.5, 2, 3, 5$.

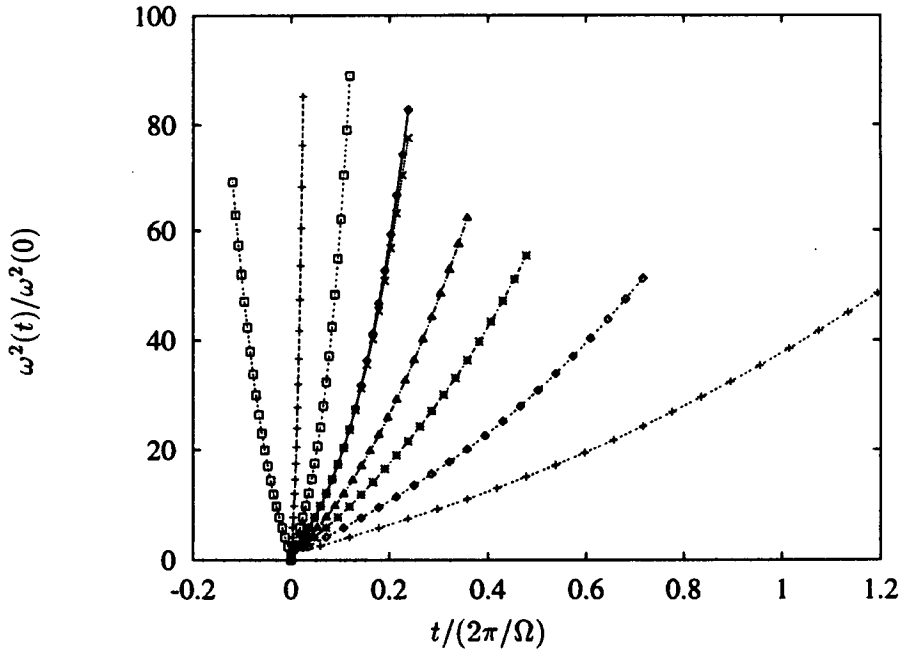


FIGURE 8. Normalized enstrophy $\omega^2(t)/\omega^2(0)$ for different values of the rotation number $2\Omega^f/S$, as a function of the non-dimensional time $t/(2\pi/\Omega^f)$ (and of t for the case $\Omega^f = 0$). Curves as in Fig. 7.

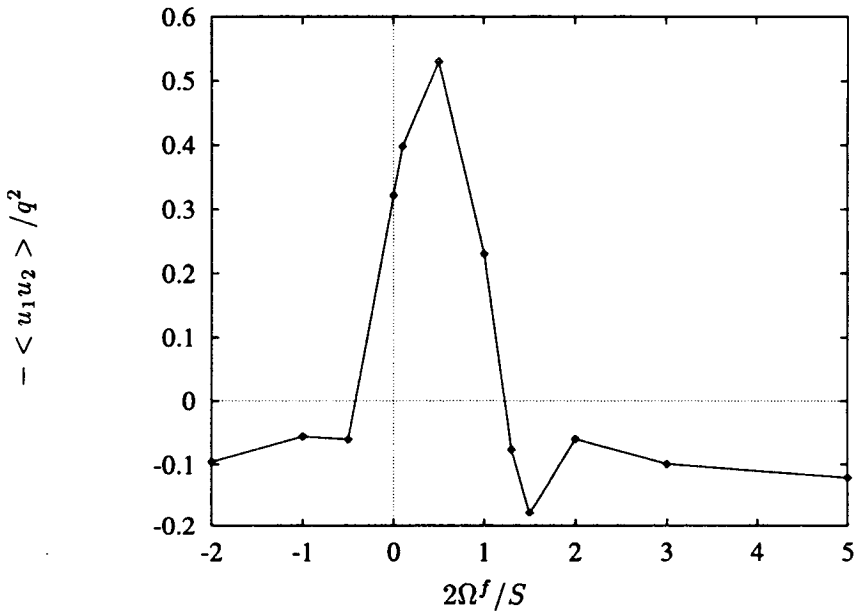


FIGURE 9. Normalized production of kinetic energy $-\langle u_1 u_2 \rangle / q^2$ at time $t = 3$ for different values of the ratio $2\Omega^f/S$.

4.2 Production of kinetic energy

Figure 9 shows the negative of the Reynolds shear stress, $-\langle u_1 u_2 \rangle$, normalized by the kinetic energy $q^2(t)$ at time t . We find that the transition zone, in terms of Ω , does not evolve smoothly in the crucial transition zone, in terms of the rotation number. The distribution of the production is not symmetric around $R = 2\Omega^f/S = 0$, since, in this case, maximum destabilization is obtained for $R = -1/2$.

4.3 Structure of rotating homogeneous shear flow

As mentioned in Section 2.2, the equations for the RDT approximation can be solved for wave vectors evenly distributed on a cube in spectral space. A resolution of 32^3 points has been chosen, and an initial isotropic fluctuating velocity field has been built using random Fourier modes (see Rogallo, 1981). By computing the time evolution of this velocity field, submitted to the mean shear, and to different values of the rotation rate, one can see qualitatively the structure of the flow. Figures 10, 11, and 12 show the isolines of the streamwise component of the velocity in a given plane of constant mean velocity and at different times, *i.e.* different cumulative distortions.

It can be seen that the case at maximum *destabilizing* rotation rate $\Omega^f = 5$ in Fig. 12 has rapidly elongating structures that align with the streamwise direction. For the intermediate destabilizing value of the rotation, $\Omega^f = 2$, the structures still align in this direction, but elongate somehow less, and more slowly, even at the quite high cumulative distortion rate $St = 2D = 10$. We notice by comparing the plots at the intermediate value $St = 5$ that one has to wait for the full deformation

(symmetric and anti-symmetric parts) to play a role before having a full characterization of the most destabilizing case (Fig. 12). Finally, the stabilizing case at $\Omega^f = -2$ presents a different pattern at the same last value of $St = 10$, and the intermediate states at $St = 2.5$ and $St = 5$ are clearly closer to the isotropic case than those in Fig. 12. For identifying the different cases, which is *a priori* not obvious, one has to look at the characteristic length of the black patches on the iso-contours plots. Figure 12 presents almost no such region, whereas Fig. 10 exhibits longer “structures” in darker regions than the stabilized case in Fig. 11. Nevertheless, the — still subjective — interpretation of such a representation has to be completed with statistical indicators of the anisotropy.

For this purpose, we can also introduce here the 2D energy components $\mathcal{E}_{ij}^l = \langle u_i u_j \rangle L_{ij}^l$, as the product of the Reynolds stress tensor components with a corresponding integral length scale (Salhi & Cambon, 1995b). These quantities may be a better indicator for looking at the anisotropy in the flow than each of the Reynolds stress or the integral length separately, since both the anisotropy of $\langle u_i u_j \rangle$ and L_{ij}^l play a role in \mathcal{E}_{ij}^l . For example, in the inviscid case, it is possible to get *analytical* solutions for the evolution of most of these energy components in the case of a homogeneous shear flow, but not for L_{ij}^l separately. The “eddy elongation parameter”, *i.e.* the ratio $\kappa = L_{11}^1/L_{11}^3$ can be computed from these since it is also $\kappa = \langle u_1 u_1 \rangle L_{11}^1 / (\langle u_1 u_1 \rangle L_{11}^3) = \mathcal{E}_{11}^1 / \mathcal{E}_{11}^3$. A large value of κ indicates the stretching of the structures. For instance, for $R = 2\Omega^f/S = 2$, a stabilized case, $\kappa \simeq 0.7$, whereas for $R = -2$, the destabilized case, $\kappa \simeq 1.3$, both at the same given instant $St = 10$. And for the case of zero absolute vorticity $R = 1$, the ratio *remains constant*. These three cases are close to the situations presented in three planes in a rotating channel flow (see Section 5), where the destabilized, stabilized, and middle regions are represented. (Of course, when comparing different energy components, one has to be aware that different components of the Reynolds stress tensor can be involved, as well as that opposite tendencies on $\langle u_i u_j \rangle$ and L_{ij}^l could leave \mathcal{E}_{ij}^l almost unchanged.)

Finally, it is interesting to notice that the *symmetric* part of the deformation tensor \overline{G} has its eigenvectors oriented at an angle of $\pi/4$ radians to the streamwise direction. Accordingly, at the first stage of the evolution, the flow structures tend to be aligned with this orientation. Of course, for later stages in time, the full role of the deformation is a stretching in the direction of the mean flow.

5. LES of a rotating channel flow

In this section, we consider results from 128^3 direct numerical simulations performed at NASA Ames Research Center by Kim. The reader is referred to Lee *et al.* (1990) for all the details of the numerical method. A stationary velocity field is obtained in a channel between two parallel plane walls, which is located in a frame rotating around the spanwise direction. The streamwise direction is x , the spanwise direction is z , and the (inhomogeneous) vertical direction is y . The mean velocity profile (shown in Fig. 13) induces a shear that depends on the transverse coordinate (perpendicular to the walls). Therefore, the previous homogeneous stability

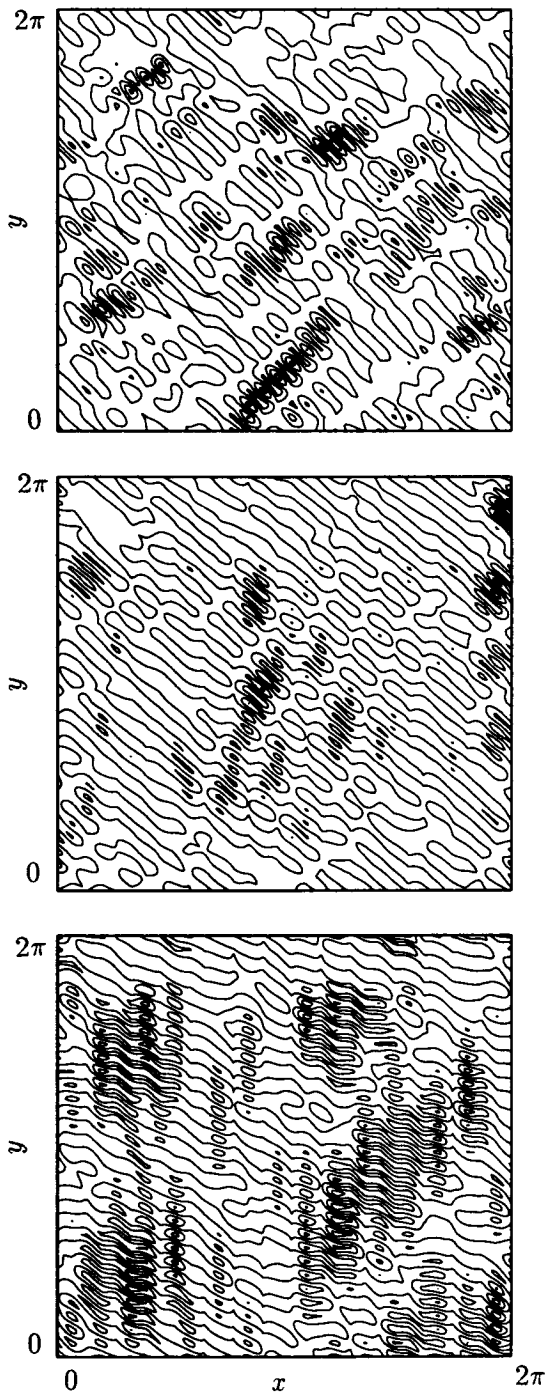


FIGURE 10. Isolines of u_x component of fluctuating velocity at $Dt = 2.5, 5, 10$ from top to bottom at mid-height in the periodic computational box of homogeneous isotropic turbulence. The rotation number is $2\Omega^f/S = 2$.

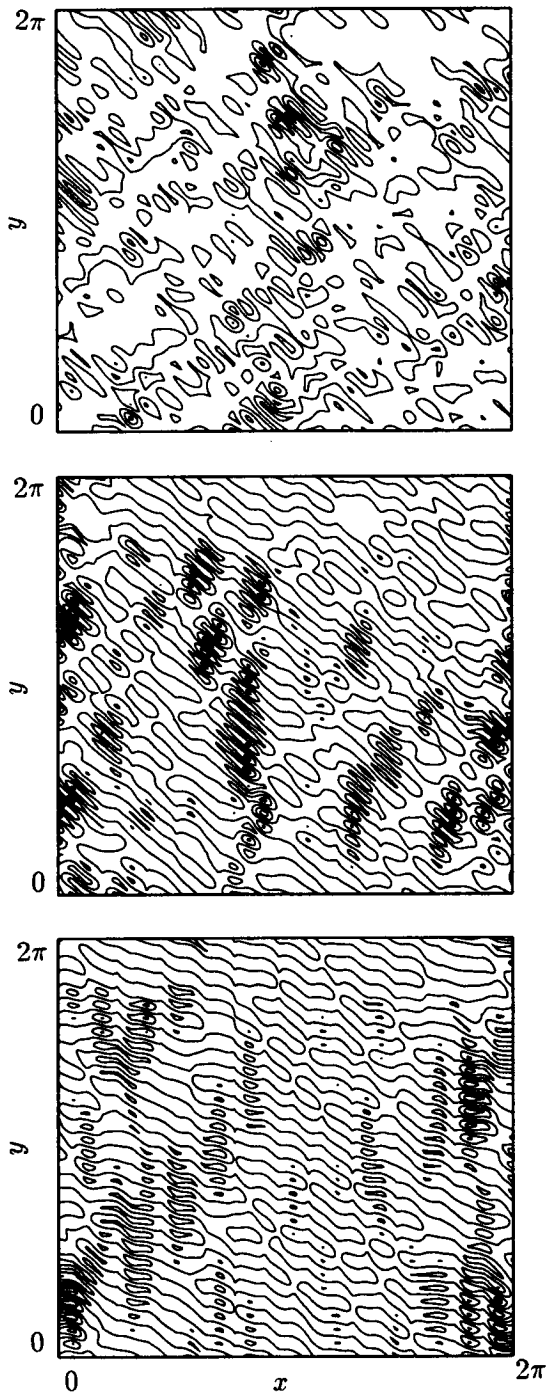
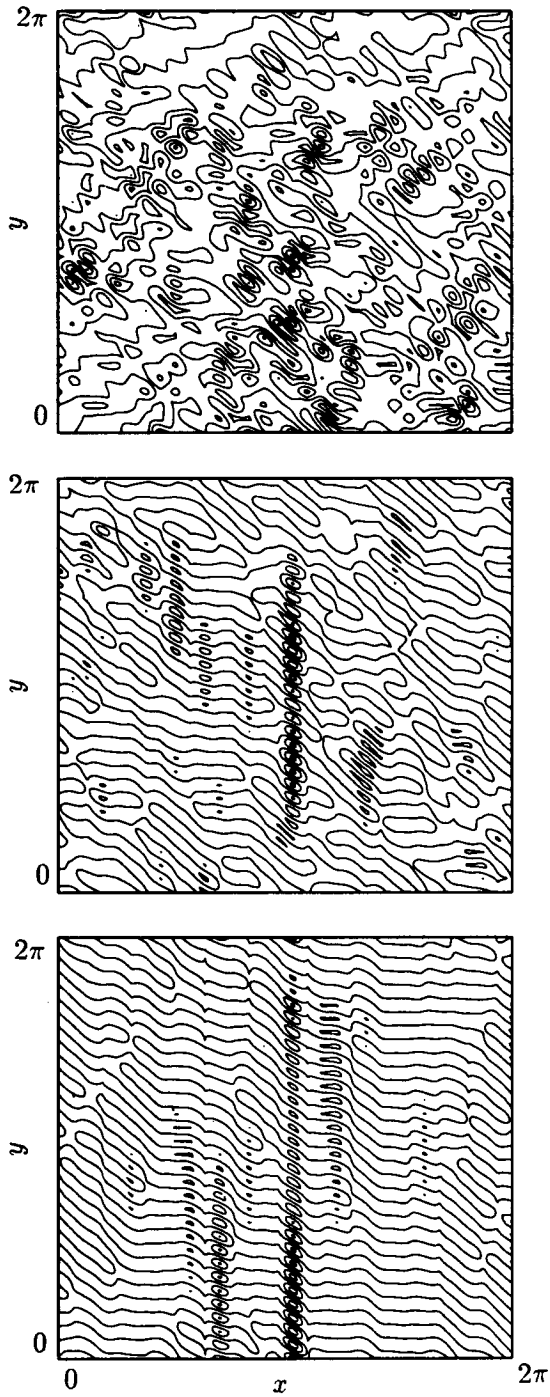


FIGURE 11. Same as Fig. 10 with $2\Omega^f/S = -2$.

FIGURE 12. Same as Fig. 10 with $2\Omega^f/S = 5$.

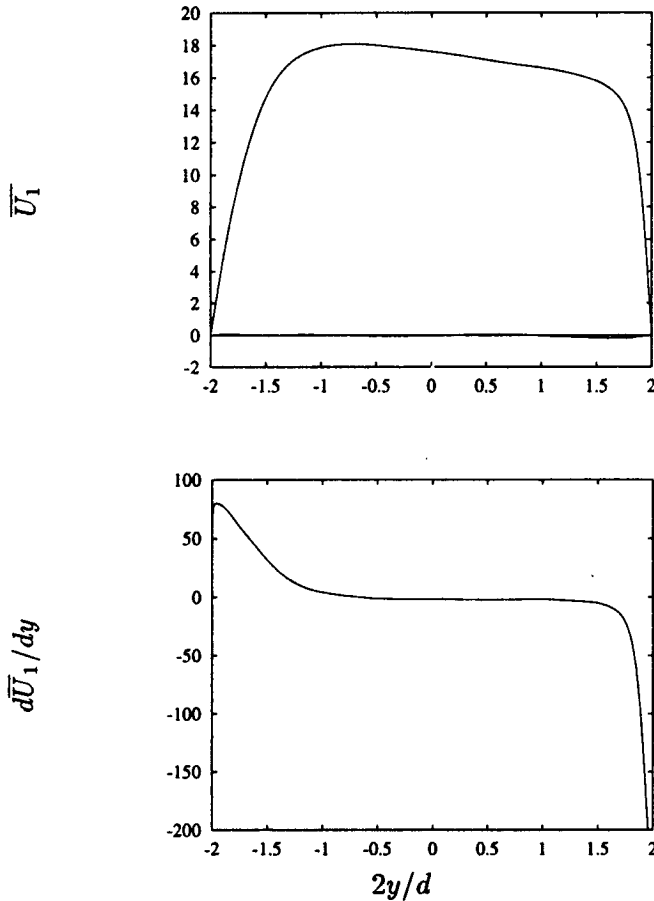


FIGURE 13. Mean velocity profile of \bar{U}_1 in the rotating channel (top figure), and corresponding shear $d\bar{U}_1/dy$ (bottom figure). On top figure the other components \bar{U}_2 and \bar{U}_3 are almost zero.

analysis of rotating shear flows can be compared, in terms of anisotropy, to the turbulence in different planes in the rotating channel flow where the mean shear is constant. Experimental and numerical investigations (Johnston *et al.*, 1972, Watmuff *et al.*, 1985, Kristoffersen & Andersson, 1993) have shown the particular role of the rotation onto different regions in the channel, namely the modification of the mean velocity profile, with a destabilization of the flow close to the pressure wall (negative shear), and a stabilization near the suction wall (positive shear). The latter effect eventually leads to a *relaminarization* of the flow in the corresponding region.

Figure 14 gathers the distribution of the Reynolds stress tensor components. The lack of symmetry is evident, with enhanced components of the fluctuating velocity towards the destabilized wall; the production $-\langle u_1 u_2 \rangle$ of kinetic energy changes sign when moving from one wall to the other. This can be related to a similar effect shown in Fig. 9, where the production for the homogeneous case is plotted versus

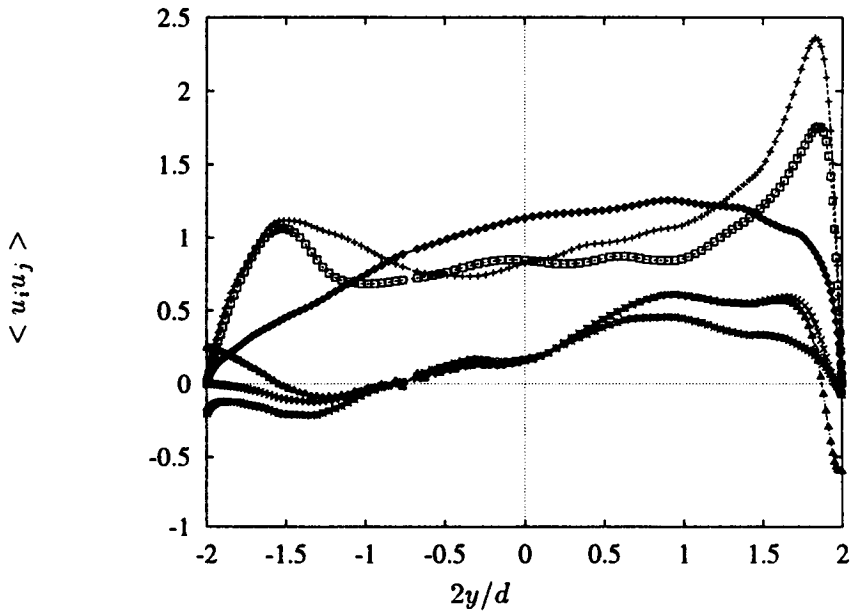


FIGURE 14. Variation of the components of the Reynolds stress tensor with the distance to the wall. $\langle u_1^2 \rangle$: +, $\langle u_2^2 \rangle$: \diamond , $\langle u_3^2 \rangle$: \square , $\langle u_1 u_2 \rangle$: \times , $\langle u_1 u_3 \rangle$: *, $\langle u_2 u_3 \rangle$: \triangle .

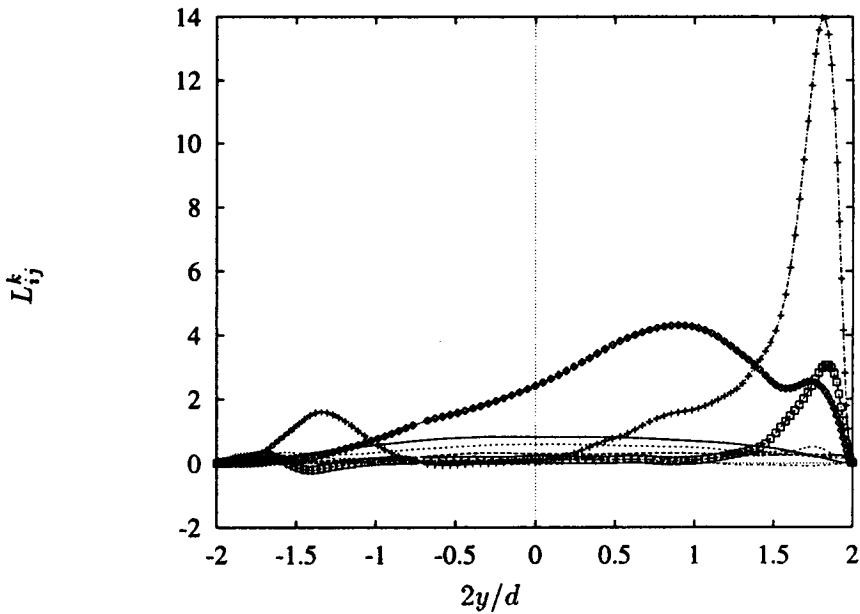


FIGURE 15. Variation of the integral length scales with the distance to the wall. L_{22}^x : \diamond , L_{11}^x : +, L_{33}^x : \square , L_{22}^y : —, L_{33}^y : - - - .

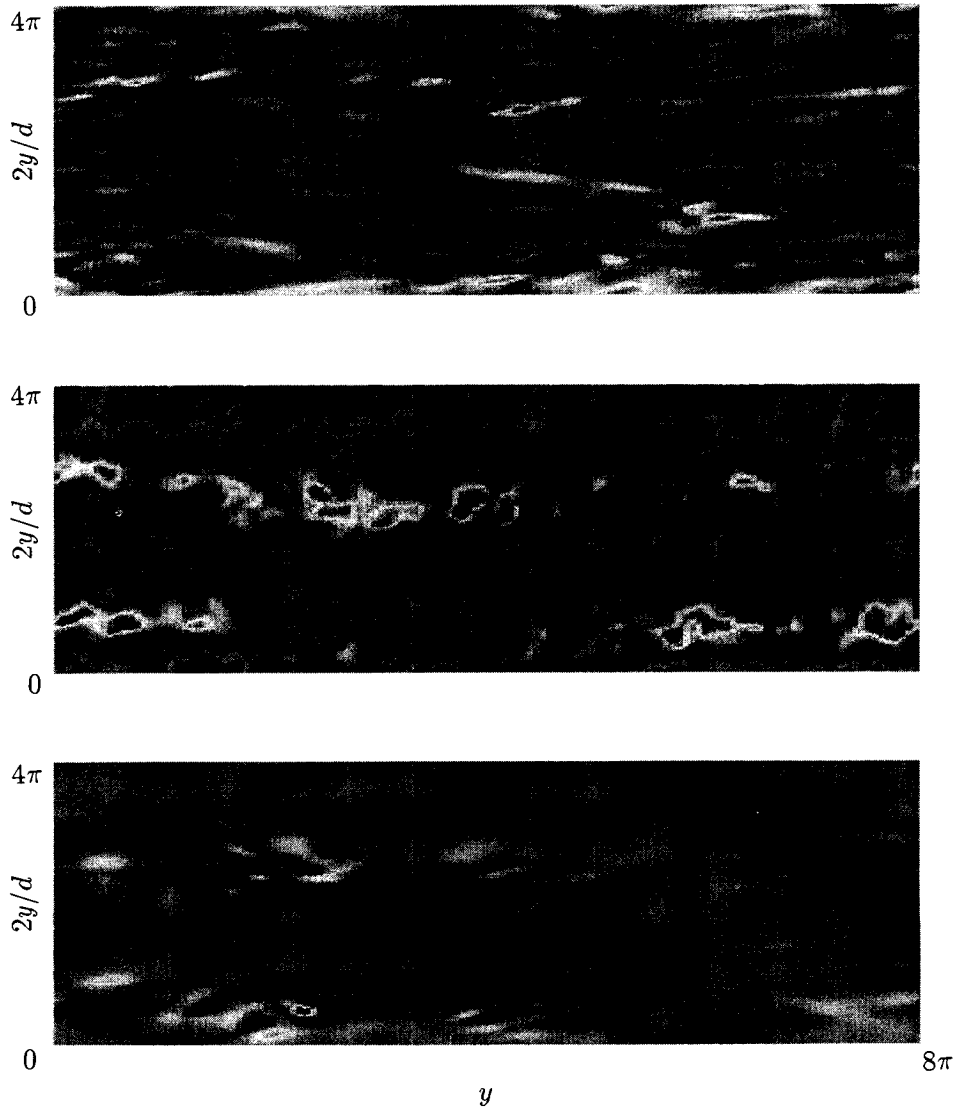


FIGURE 16. Iso-surfaces of the streamwise component of the velocity in the planes $2y/d = 1.95, 0, -1.95$, figures from top to bottom, in the rotating channel.

$2\Omega^f/S$. In the DNS channel, the modification of this ratio results from the variation of S with the distance to the walls.

Distributions of the fluctuating velocity field exhibit different patterns depending on the distance to the wall. Figure 16 shows the iso-surfaces of the streamwise component u_x in planes parallel to the walls, in the stabilized, middle and destabilized regions. One sees immediately that the level of turbulence in the destabilized region is much higher than that in the other ones (see also the variance of the components u_i in Fig. 14). Moreover, the destabilized region presents structures clearly

elongated in the streamwise direction, *as in the homogeneous case*. It is interesting to compute the corresponding integral length scales to evaluate quantitatively the anisotropy of these structures and how much they are stretched in the different planes. Figure 15 shows the integral length scales

$$L_{ij}^k = \int_0^\infty dx_k \langle u_i u_j \rangle(x_k) / \langle u_i u_j \rangle(0),$$

where ij shows which components of the fluctuating velocity are taken into account, and k shows the direction of separation. Obviously, the most striking feature of this figure is the very large increase of L_{11}^x that confirms the elongation of the structures, maximum at $x = 1.8$, in the region of maximum mean shear. The tendency is somewhat smaller for the transverse correlation L_{33}^x , but an interesting fact is that the transverse correlation length for u_y has its maximum displaced towards the center of the channel. The quite large value of the mean shear close to the stabilized wall is also responsible for the (small) peak of L_{11}^x , no matter the stabilizing effect of the rotation in this particular case. Here, we notice that the qualitative predictions of RDT applied to the homogeneous shear flow with rotation agree with the distributions of the integral length scales in the channel flow. Indeed, the general streak-like structures appear in the homogeneous RDT results, and the rotation affects the different regions in the same way equivalent regions of homogeneous rotating turbulence with the same value of R (as in Section 4.3) are affected.

6. Future plans

In light of the results presented in this summary, it will be interesting to refine the study by investigating quantitatively the different parameters of both the homogeneous rotating shear flow and the rotating channel flow. DNS computations with different rotation rates, if available, would be a valuable database for comparison, at the level of one-point statistics, with the equivalent RDT approach. The modeling of the anisotropy in the flow, especially through the evolution of the integral length scales as well as the anisotropy tensors, will probably benefit from such studies. Finally, one can investigate if the Coriolis force, due to the rotation of the frame, could be an analog of the centrifugal acceleration in curved flows. Since the RDT approximation can be closely related to stability analyses, we can try to see if and how the streak-like structures in the rotating channel can be matched to Görtler vortices due to curvature.

Acknowledgments

The author is indebted to John Kim who made available his LES simulations. He also wishes to thank Nagi Mansour and Claude Cambon for their helpful collaboration.

REFERENCES

- BENOIT, J. P. 1992 Étude expérimentale et théorique d'une turbulence homogène soumise à des effets couplés de rotation et de déformation plane. Ph.D. Thesis.

- BRADSHAW, P. 1969 The analogy between streamline curvature and buoyancy in turbulent shear flow. *J. Fluid Mech.* **36**, 177–191.
- CAMBON, C. 1982 Étude spectrale d'un champ turbulent incompressible soumis à des effets couplés de déformation et de rotation imposés extérieurement. *Thèse de doctorat d'état, Université Claude Bernard-Lyon I.*
- CAMBON, C., BENOIT, J. P., SHAO, L. & JACQUIN, L. 1994 Stability Analysis and large-eddy simulation of rotating turbulence with organized eddies. *J. Fluid Mech.* **278**, 175–200.
- CAMBON, C., TEISSÈDRE, C. & JEANDEL, D. 1985 Etude d'effets couplés de déformation et de rotation sur une turbulence homogène. *J. Méc. Théor. Appl.* **4**, 629–657.
- CRAYA, A. 1958 Contribution à l'analyse de la turbulence associée à des vitesses moyennes. *P.S.T. Ministère de l'Air, no. 345.*
- HERRING, J. R. 1974 Approach of axisymmetric turbulence to isotropy. *Phys. Fluids.* **17**, 859–872.
- JOHNSTON, J. P., HALLEEN, R.M. & LEZIUS, D.K. 1972 Effects of spanwise rotation on the structure of two-dimensional fully developed turbulent channel flow. *J. Fluid Mech.* **56**, 533.
- KRISTOFFERSEN, R. & ANDERSSON, H. I. 1993 Direct simulations of low-Reynolds-number turbulent flow in a rotating channel. *J. Fluid Mech.* **256**, 163–197.
- LEE, M. J., KIM, J. & MOIN, P. 1990 Structure of turbulence at high shear rate. *J. Fluid Mech.* **216**, 561–583.
- ROGALLO, R.S. 1981 Numerical experiments in homogeneous turbulence. *NASA Technical Memorandum.* **81315.**
- SALHI, A. & CAMBON, C. 1995a Revisiting rotating shear flow at high shear rate. Submitted to *J. Fluid Mech.*
- SALHI, A. & CAMBON, C. 1995b Stability of a plane quadratic flow in a rotating frame. Submitted to *Phys. Rev. Letters.*
- SPEZIALE, C. G., ABID R. & BLAISDELL, G. 1995 On the consistency of Reynolds stress turbulence closures with hydrodynamic stability theory. Submitted to *Phys. Fluids.*
- WATMUFF, J. H., WITT, H. T. & JOUBERT, P. N. 1985 Developing turbulent boundary layers with system rotation. *J. Fluid Mech.* **157**, 405–448.